CloudSat W-Band Radar Measurements of Surface Backscatter

S. L. Durden, *Senior Member, IEEE*, S. Tanelli, and G. Dobrowalski

***Abstract*—The authors examine the characteristics of the W-band surface backscatter cross section using data from the 94-GHz cloud profiling radar on the CloudSat mission. These data from CloudSat represent the first global measurements of surface properties at 94 GHz. The authors use these data to investigate seasonal changes in surface backscatter over both land and ocean. The authors also make use of a limited set of off-nadir data to investigate behavior of W-band backscatter from the ocean versus wind speed for incidence angles up to 17°.**

***Index Terms*—CloudSat, radar, radar scattering, surface backscatter, W-band.**

I. Introduction

THE CloudSat mission was launched in 2006 and carries a single instrument, the W-band cloud profiling radar (CPR) [1]. While designed for atmospheric observations, CPR also routinely measures the surface backscatter cross section per unit area σ° at nadir incidence. Since such measurements at 94 GHz have not been previously made on a global basis, we use CloudSat observations to derive the behavior of σ° at various locations over the Earth as a function of season. In addition to nadir operation, CPR is occasionally pointed off-nadir for calibration purposes. These data are acquired over ocean and hence provide W-band ocean surface measurements at small incidence angles (up to 17°). We present σ° versus incidence angle for several wind speed ranges.

II. CloudSat CPR

CPR is a nadir-looking W-band radar operating at a frequency of 94 GHz. Its horizontal resolution is roughly 1.4 km across track and 1.7 km along-track. The vertical (range) resolution is 500 m. In normal operation, it is pointed slightly forward (0.16°) off nadir to reduce (but not eliminate) specular return from very flat areas. Since launch in 2006, it has been providing an unprecedented view of the vertical structure of clouds on a global scale. The CPR radar was carefully calibrated with prelaunch measurements of the antenna and system losses. Instrument stability is monitored by internal telemetry and by external periodic off-nadir calibration maneuvers, as mentioned earlier. The ocean calibration maneuvers are performed every few months. The absolute calibration has been validated by statistical and direct comparisons with other ground-based and airborne radars, as described by Tanelli *et al.* [1] and Protat *et al.* [2]. These results indicate an absolute calibration accuracy of better than 2 dB and a stability of better than 0.5 dB.

CloudSat is in a 98° inclination orbit with 705-km altitude and a 16-day repeat cycle; it is part of the so-called A-Train of Earth observation satellites [3]. The data used here are derived from clear-air measurements only; no clouds or precipitation were detected in the data. The two-way gaseous attenuation correction, which can vary from less than 1 dB over the poles to 5 or more dB in the tropics [4], is derived from the CloudSat Level 2 GEOPROF product by extrapolation to the surface. Data are limited to the period after mid-August 2006, when the pointing was shifted from nadir to 0.16° forward to reduce specular reflections. The CloudSat data used here are release R04.

III. Global View of Land σ° at Nadir

Over a 16-day cycle, CPR covers nearly the entire Earth, albeit with gaps between the tracks. The data can be averaged to 5° grid spacing to produce global maps of σ° by season; these maps are shown in Figs. 1 and 2. Each $5^\circ \times 5^\circ$ box on the maps is typically an average of thousands of CPR measurements; each CPR measurement is itself an average of roughly 600 radar pulses. The actual number of CPR measurements in each box depends on the cloud/rain coverage of that box. There is little dependence on latitude; boxes at higher latitudes are smaller but get more satellite passes per area. The data in Fig. 1 are displayed over a -5 to $+15$ dB range to capture the variability in land backscatter. Fig. 2 narrows the display range to $+7$ to $+13$ dB to better show the variability in ocean surface backscatter. Note that, for convenience, we have defined season in terms of three-month periods, e.g., December, January, February is denoted by DJF. The land areas with consistently higher backscatter are the eastern U.S. and parts of Southeast Asia and India, as well as some areas in Africa and South America. As discussed in the Appendix, backscatter at nadir is likely a combination of quasi-specular scattering from the surface and volume backscatter from vegetation. Based on this, we would interpret areas with high backscattering as being flat and/or wet. This is certainly the case for the eastern versus western U.S. Not surprisingly, seasonal variability is most evident at high latitudes, including eastern Canada, the Arctic, and Antarctica. The backscatter near the poles in some areas

Manuscript received February 14, 2010; revised June 7, 2010; accepted August 7, 2010. Date of publication November 8, 2010; date of current version April 22, 2011. This work was supported in part by the CloudSat Project and in part by the CloudSat/CALIPSO Science Program.

The authors are with the Jet Propulsion Laboratory, California Institute of Technology, Pasadena, CA 91109 USA (e-mail: sdurden@jpl.nasa.gov; simone.tanelli@jpl.nasa.gov; gregg.dobrowalski@jpl.nasa.gov).

Color versions of one or more of the figures in this paper are available online at http://ieeexplore.ieee.org.

Digital Object Identifier 10.1109/LGRS.2010.2079314

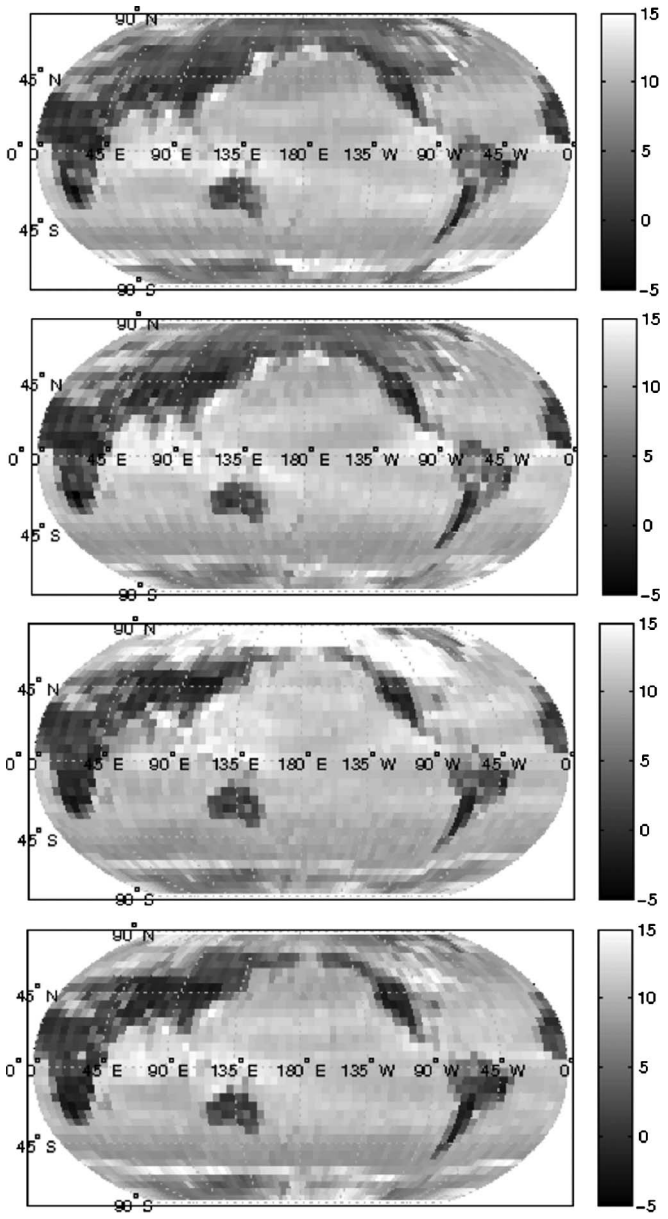

Fig. 1. Maps of W-band nadir σ° (in decibels) over the Earth's surface by season. The top image is DJF, followed by MAM, JJA, and SON at bottom.

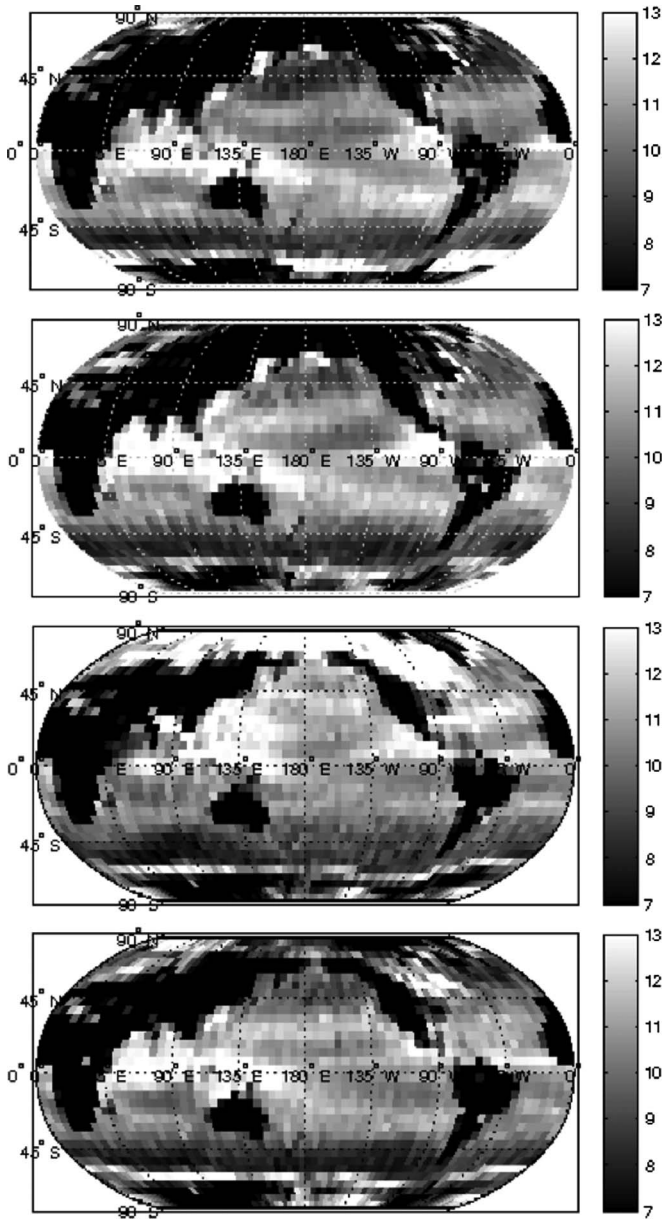

Fig. 2. Same data as in Fig. 1, except that the range of display has been reduced for best contrast in ocean surface σ° (in decibels). As with Fig. 1, top is DJF followed by MAM and JJA. Bottom is SON. Land surface is mostly saturated with this display scale.

is noticeably stronger in summer due to surface water specular reflection, as discussed in more detail in the next section.

Backscatter at nadir from the oceans (without ice) should be entirely due to the quasi-specular mechanism [5]. Areas with high backscatter are thus flatter and associated with lower winds, for example, the northern Indian Ocean in autumn (SON). Low backscatter, in contrast, is associated with high winds, as indicated by the darker band in the southern ocean, north of Antarctica, and the northern Pacific Ocean in winter. The western Pacific is also darkest during DJF. The higher average wind in winter in the northern and western Pacific is likely due to the strong extratropical cyclones that move off the coast of Asia in winter. While typhoons in summer and autumn can have higher wind speeds, they are more localized and less frequent, causing less impact on average wind speed. The North Atlantic's behavior is similar. The tropical eastern Pacific appears calmest in spring and summer. The bright feature between the southern oceans and the landmass of Antarctica marks the extent of the ice-covered ocean; liquid water on top of the ice creates extremely bright returns due to specular reflection, as will be discussed hereinafter in more detail.

IV. Nadir σ° for Selected Sites

We have selected several sites over the Earth to examine statistics of σ° by season. Table I lists the selected sites, which range from prairie in the midwestern U.S. to rain forest to sea ice and open ocean. North latitude and east longitude are defined to be positive. Included in Table I is an estimate of the area of each study site. Table II presents the mean σ° for each of these sites as a function of season, while Table III presents

TABLE I
LIST OF REGIONS USED IN THIS STUDY

Region	Lat (deg)	Lon (deg)	Area (10^5 km^2)
Amazon	-8.5	-55.0	6.0
Canada-forest	60.0	-101.0	4.9
Kansas	37.5	-95.0	4.9
Sahara	20.0	15.0	22.9
Antarctica	-77.4	12.5	3.3
Weddell	-65.0	0.0	5.2
Baffin	72.0	-64.0	2.6
Atlantic-mid	36.6	-43.1	4.8
Atlantic-tropical	15.0	-45.0	11.8

TABLE II
MEAN OF σ°

Region	DJF	MAM	JJA	SON
Amazon	4.1	5.0	2.1	0.9
Canada-forest	5.5	6.3	15.8	12.0
Kansas	8.3	10.0	8.3	6.9
Sahara	1.0	1.0	1.1	1.0
Antarctica	9.7	11.0	10.7	9.9
Weddell	12.7	12.1	8.7	8.9
Baffin	7.4	8.0	16.8	12.6
Atlantic-mid	9.8	10.4	12.5	10.8
Atlantic-tropical	10.1	10.4	10.8	11.5

TABLE III
STANDARD DEVIATION OF σ°

Region	DJF	MAM	JJA	SON
Amazon	6.7	6.7	6.1	6.3
Canada-forest	2.6	4.9	5.1	6.5
Kansas	6.0	5.8	6.1	6.1
Sahara	3.0	3.1	3.4	3.2
Antarctica	2.3	2.2	2.0	2.4
Weddell	5.2	5.3	5.4	5.3
Baffin	5.6	6.0	5.7	5.2
Atlantic-mid	2.2	2.1	2.9	2.2
Atlantic-tropical	1.5	1.3	1.4	1.8

the corresponding standard deviations. Table IV provides the number of CPR measurements used in calculating the numbers in Tables II and III; it shows that the number of available clear-air samples can vary significantly with season. Three years worth of data, starting in August 2006, were used in deriving these tables.

The Amazon rainforest has a backscatter that peaks in the rainy season (MAM) and reaches a minimum in the dry season (SON). While this could be a vegetation effect, it could also be related to surface water causing a specular contribution. As described in the Appendix, the specular cross section of a patch of water depends on the square of the water area and would add to the quasi-specular land surface component in (A1). A more extreme seasonal effect can be seen in the boreal forest in Canada, with σ° peaking in the summer (JJA). The standard deviation during JJA is double that of DJF and similar to the Amazon. Again, we suspect standing water; its presence or absence would cause large changes in σ° leading to the large

TABLE IV
NUMBER OF CLOUDSAT MEASUREMENTS FOR EACH LOCATION AND SEASON ($\times 10^4$)

Region	DJF	MAM	JJA	SON
Amazon	2.8	4.0	8.9	5.7
Canada-forest	9.1	8.9	8.8	7.3
Kansas	6.1	6.1	6.9	7.3
Sahara	36.5	35.2	36.6	38.9
Antarctica	25.9	23.5	25.0	24.8
Weddell	5.8	4.9	7.2	7.4
Baffin	6.4	6.1	7.3	4.1
Atlantic-mid	4.2	5.0	7.8	5.5
Atlantic-tropical	13.2	15.1	13.8	12.9

standard deviation. The CPR measurements for the wet season are larger than might be expected for vegetation, based on measurements in [6], further supporting the hypothesis that the large wet season measurements are due to surface water. The backscatter from the midwestern U.S. prairie (Kansas) shows less dependence on season, with the standard deviation being nearly constant. The maximum in spring may be due to a shift from surface backscatter in the winter to vegetation backscatter in the summer. When no vegetation is present, as in the case of the Sahara, σ° is nearly constant with season.

While some variability occurs for Antarctica, larger variation is found for the Weddell Sea near Antarctica and the Baffin Bay just off Greenland. The peak σ° is likely due to the presence of melt ponds (standing water) [7] in the summer months (for that hemisphere), giving rise to nearly specular reflection, as also noted previously for high latitudes. Specular mirrorlike reflection requires a surface that is nearly normal to the incident radar beam, as described in the Appendix. Fig. 3 shows CloudSat-measured scattering at three angles: the initial 1.7° incidence, exact nadir, and 0.16° off nadir. The large increase in return when moving to nadir shows the importance of specular reflection; the angular dependence of quasi-specular scattering is much weaker than for specular reflection.

The open ocean areas, in contrast to land areas, do not have large variation in backscatter, particularly in the tropics. The larger variability of land backscatter relative to ocean backscatter at nadir was also seen at 13.8 GHz [8]. The maximum value of σ° for the midlatitude Atlantic occurs in summer (JJA). An examination of the surface wind estimate from the AMSR-E on the Aqua mission indicates that the wind speed reaches a minimum for that same period. This behavior is consistent with quasi-specular scattering at nadir. The tropical Atlantic σ° behavior is somewhat similar to that of the midlatitude site but with the maximum backscatter occurring in SON. The largest standard deviation for the tropical Atlantic also occurs during the fall (SON), instead of summer.

V. OFF-NADIR OCEAN σ°

While the vast majority of CloudSat data are acquired at nadir, CloudSat has performed a number acquisitions with the spacecraft rolled to one side by up to 15° (resulting in incidence angles at the surface up to 17°). These acquisitions have been done over the ocean with the goal of using the ocean

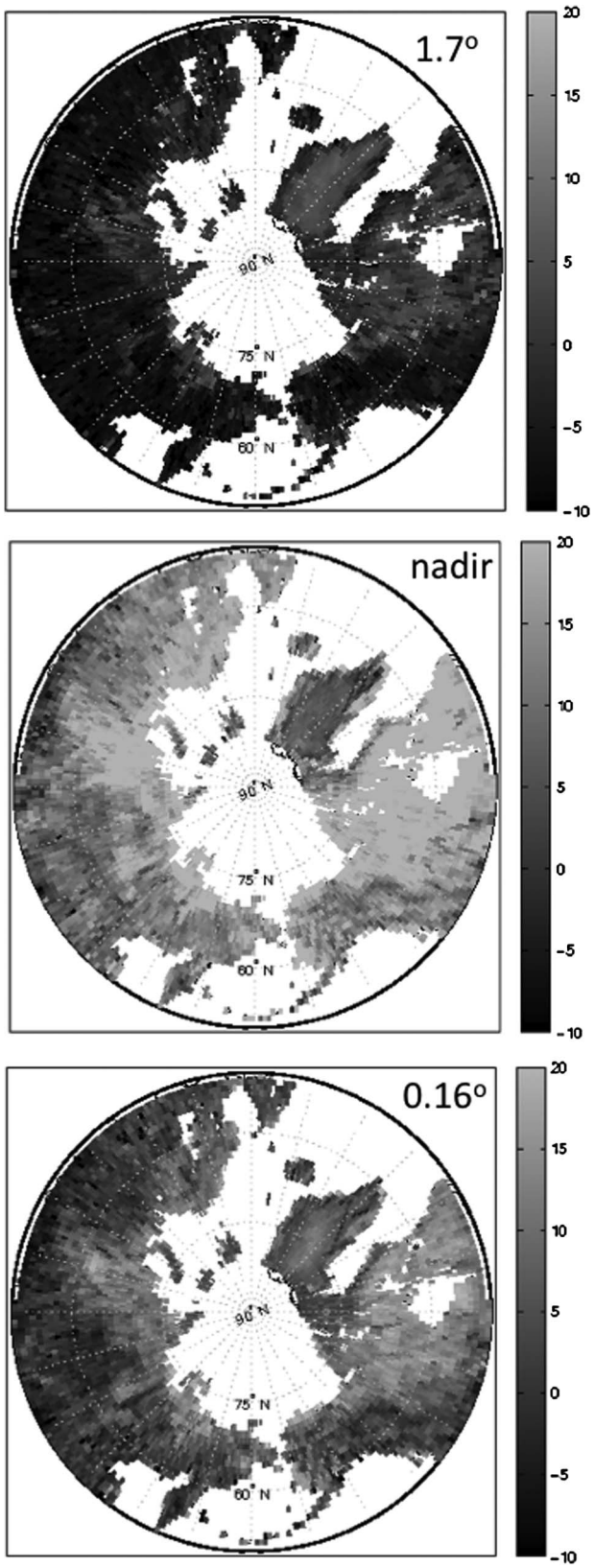

Fig. 3. CloudSat-measured high-latitude land σ° (not corrected for attenuation) at the three incidence angles used for CloudSat during early orbit operations. Colorbar is in decibels.

as a calibration target [1], [5]. Due to operational constraints, most of these acquisitions have taken place in the Southern Hemisphere, frequently in the Indian Ocean west of Australia.

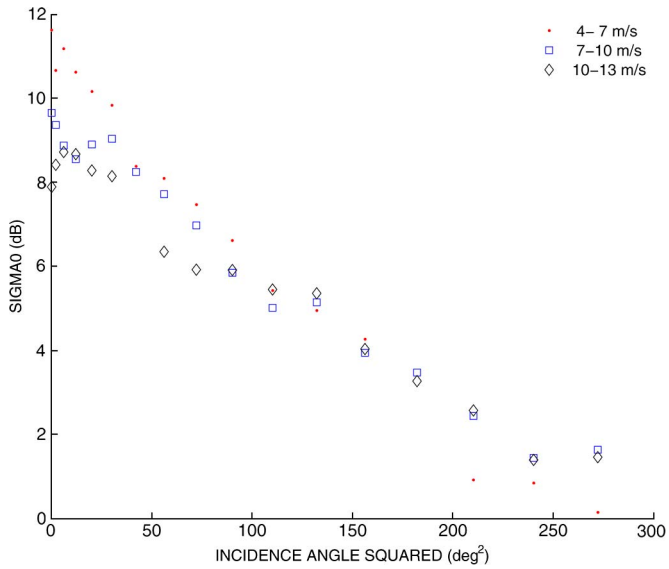

Fig. 4. CloudSat-measured ocean σ° versus the square of the incidence angle for several wind speed categories.

The wind speeds during the various acquisitions, as obtained from AMSR-E, range up to 13 m/s. Cases with wind speeds less than 4 m/s were infrequent and were excluded from this study; in these cases, the ocean scattering becomes intermittent and may not obey the statistics needed for quasi-specular scattering. There is no Level 2 GEOPROF product for these data, so attenuation correction is done using atmospheric reanalysis data. Over ocean, this correction differs by less than 1 dB from the correction used in the previous sections. The observed σ°, after correction for gaseous attenuation, has an incidence angle dependence shown in Fig. 4. There, we plot as a function of incidence angle squared rather than just incidence angle, based on the form of quasi-specular scattering in (A2). For small angles, (A2) predicts an approximately linear relation between σ° in decibels and angle squared. The CPR data have been classed into three wind speed categories, based on the colocated AMSR-E wind speed measurements. Equation (A2) predicts decreasing nadir σ° and increasing σ° away from nadir as the wind speed increases, increasing the surface slope variance S^2. This agrees with Fig. 4, which shows a reduced slope in the σ° versus incidence-angle-squared relationship at higher wind speeds. We performed linear regressions for each of the wind speed classes and found the following regression line slopes: -0.043 dB/deg^2 at 4–7 m/s, -0.032 dB/deg^2 at 7–10 m/s, and -0.028 dB/deg^2 at 10–13 m/s, confirming our impressions from Fig. 4.

The dependence of the regression line slope (σ° versus angle squared) has been investigated previously for measurements at Ku- and Ka-bands [9]. There, it was found that the Ka-band regression line slopes drop below the Ku-band slopes starting around -0.05 dB/deg^2 with increasing difference for higher wind speeds. This was noted in [9] as being a result of scattering from an effective surface rather than the full surface. Specifically, that part of the surface spectrum with scale smaller than the electromagnetic wavelength should not contribute to quasi-specular scattering. Hence, as the electromagnetic wavelength is reduced, the surface looks rougher. This would tend to reduce

the slope of the regression line as frequency increases. It might be expected that the regression line slope at W-band would be even smaller than Ka-band, but simultaneous Ka- and W-band data are really needed to confirm this. Our data do, however, show that the W-band regression line slopes are in a similar range as the slopes found in [9].

APPENDIX

The nadir σ° of a natural target is assumed to be due to a rough surface with a possible vegetation layer above it; this is similar to other radar models (e.g., [10]). A simple model using quasi-specular surface scattering [11] and volume scattering (e.g., [12]) from a vegetation layer of thickness H is

$$\sigma^\circ = \frac{R^2}{S^2} e^{-2kH} + \frac{\eta}{2k}(1 - e^{-2kH}) \tag{A1}$$

where R^2 is the plane surface power reflection coefficient, S^2 is the total surface slope variance, k is the vegetation attenuation coefficient, and η is the vegetation backscatter cross section per unit volume. The R^2/S^2 factor in the first term is the nadir quasi-specular σ°, while the exponential factor accounts for attenuation of the surface scattering by the vegetation layer of depth H. The second term is the volume scattering term; as the vegetation density increases, both η and k increase. This will eventually result in domination of volume scattering relative to surface scattering. As k increases, the vegetation scattering comes from a thinner layer at the top of the vegetation, limiting the growth of this term. Not included here is volume scattering from inhomogeneous regions below the surface, which could be important in some areas.

Quasi-specular scattering refers to reflection from those portions of a randomly rough surface that happen to be directly facing the radar. A very smooth water surface (relative to the wavelength) does not act like many small facets but rather as one large mirror. Hence, for standing water, we should add specular reflection to (A1). The radar cross section of a flat plate with area A is $4\pi A^2/\lambda^2$, so even a small patch of water can have an extremely large radar cross section, if the water surface aligns exactly perpendicular to the geodetic nadir vector. In fact, a flat surface of a few hundred square meters encountered at any point during the 0.16-s integration time, along the radar boresight ground track, is sufficient to dominate the backscattered signal from a land surface. As the angle of the propagation vector relative to the plate's normal increases, backscatter decreases dramatically. This was observed at high latitudes when the CPR pointing was changed from nadir to 0.16°. Even so, the specular component can still be significant in some cases. The impact of specular returns and their strong dependence on the incidence angle are evident in the data acquired by CloudSat in the summer of 2006 shown in Fig. 3.

For ocean scattering near nadir, quasi-specular scattering alone should be a good description. At much larger angles from nadir, two-scale scattering models that combine quasi-specular and Bragg scattering are needed (e.g., [13]). Since all our data are within 15° off nadir, the ocean backscatter cross section is modeled using just the quasi-specular term from (A1) but modified for a range of incidence angles:

$$\sigma^\circ = \frac{R^2}{S^2} \sec^4\theta e^{-\tan^2\theta/S^2} \tag{A2}$$

where θ is the incidence angle relative to nadir.

ACKNOWLEDGMENT

This study was carried out at the Jet Propulsion Laboratory, California Institute of Technology, under a contract with the National Aeronautics and Space Administration.

REFERENCES

[1] S. Tanelli, S. L. Durden, E. Im, K. S. Pak, D. G. Reinke, P. Partain, J. M. Haynes, and R. T. Marchand, "CloudSat's cloud profiling radar after two years in orbit: Performance, external calibration, and processing," *IEEE Trans. Geosci. Remote Sens.*, vol. 46, no. 11, pp. 3560–3573, Nov. 2008.

[2] A. Protat, D. Bouniol, J. Delanoë, E. O'Connor, P. T. May, A. Plana-Fattori, A. Hasson, U. Görsdorf, and A. J. Heymsfield, "Assessment of Cloudsat reflectivity measurements and ice cloud properties using ground-based and airborne cloud radar observations," *J. Atmos. Ocean. Technol.*, vol. 26, no. 9, pp. 1717–1741, Sep. 2009.

[3] G. L. Stephens, D. G. Vane, R. J. Boain, G. G. Mace, K. Sassen, Z. Wang, A. J. Illingworth, E. J. O'Connor, W. B. Rossow, S. L. Durden, S. D. Miller, R. T. Austin, A. Benedetti, and C. Mitrescu, "The CloudSat mission and the A-train: A new dimension of space-based observations of clouds and precipitation," *Bull. Amer. Meteorol. Soc.*, vol. 83, no. 12, pp. 1771–1790, Dec. 2002.

[4] R. Marchand, G. G. Mace, T. Ackerman, and G. Stephens, "Hydrometeor detection using CloudSat—An earth-orbiting 94-GHz cloud radar," *J. Atmos. Ocean. Technol.*, vol. 25, no. 4, pp. 519–533, Apr. 2008.

[5] L. Li, G. M. Heymsfield, L. Tian, and P. E. Racette, "Measurements of ocean surface backscattering using an airborne 94-GHz cloud radar—Implication for calibration of airborne and spaceborne W-band radars," *J. Atmos. Ocean. Technol.*, vol. 22, no. 7, pp. 1033–1045, Jul. 2005.

[6] F. T. Ulaby and M. C. Dobson, *Handbook of Radar Scattering Statistics for Terrain*. Norwood, MA: Artech House, 1989.

[7] P. D. Taylor and D. L. Feltham, "A model of melt pond evolution on sea ice," *J. Geophys. Res., Oceans*, vol. 109, C12007, Dec. 2004. DOI: 10.1029/2004JC002361.

[8] R. Meneghini, T. Iguchi, T. Kozu, L. Liao, K. Okamoto, J. A. Jones, and J. Kwiatkowski, "Use of the surface reference technique for path attenuation estimates from the TRMM precipitation radar," *J. Appl. Meteorol.*, vol. 39, no. 12, pp. 2053–2070, Dec. 2000.

[9] S. Tanelli, S. L. Durden, and E. Im, "Simultaneous measurements of Ku- and Ka-band sea surface cross-sections by an airborne radar," *IEEE Geosci. Remote Sens. Lett.*, vol. 3, no. 3, pp. 359–363, Jul. 2006.

[10] S. L. Durden, J. J. van Zyl, and H. A. Zebker, "Modeling and observation of the radar polarization signature of forested areas," *IEEE Trans. Geosci. Remote Sens.*, vol. 27, no. 3, pp. 290–301, May 1989.

[11] D. E. Barrick, "Rough surface scattering based on specular point theory," *IEEE Trans. Antennas Propag.*, vol. AP-16, no. 4, pp. 449–454, Jul. 1968.

[12] R. H. Lang and J. S. Sidhu, "Electromagnetic backscattering from a layer of vegetation—A discrete approach," *IEEE Trans. Geosci. Remote Sens.*, vol. GRS-21, no. 1, pp. 62–71, Jan. 1983.

[13] S. L. Durden and J. F. Vesecky, "A physical radar cross-section model for a wind-driven sea with swell," *IEEE J. Ocean. Eng.*, vol. OE-10, no. 4, pp. 445–451, Oct. 1985.